Modeling and Optimization of Solar Thermoelectric Generators for Terrestrial Applications

Daniel Kraemer[a,1], Kenneth McEnaney[a,1], Matteo Chiesa[b,a], Gang Chen[a,*]

[a] *Department of Mechanical Engineering, Masschusetts Institute of Technology, Cambridge, MA 02139*
[b] *Laboratory for Energy and Nano-Science, Masdar Institute of Science and Technology, PO Box 54224, Abu Dhabi, UAE*

Abstract

In this paper we introduce a model and an optimization methodology for terrestrial solar thermoelectric generators (STEGs). We describe, discuss, and justify the necessary constraints on the STEG geometry that make the STEG optimization independent of individual dimensions. A simplified model shows that the thermoelectric elements in STEGs can be scaled in size without affecting the overall performance of the device, even when the properties of the thermoelectric material and the solar absorber are temperature-dependent. Consequently, the amount of thermoelectric material can be minimized to be only a negligible fraction of the total system cost. As an example, a Bi_2Te_3-based STEG is optimized for rooftop power generation. Peak efficiency is predicted to be 5% at the standard spectrum AM1.5G, with the thermoelectric material cost below 0.05 $\$/W_p$. Integrating STEGs into solar hot water systems for cogeneration adds electricity at minimal extra cost. In such cogeneration systems the electric current can be adjusted throughout the day to favor either electricity or hot water production.

Keywords:
solar power conversion, terrestrial solar thermoelectric generator, flat-panel, design optimization, large thermal concentration, solar thermoelectric cogeneration

*Corresponding author at: Massachusetts Institute of Technology, 77 Massachusetts Ave., (3-260), Cambridge, MA 02139, USA. Tel.: 001 (617) 253-006; Fax.: 001 (617) 258-5802; Email: gchen2@mit.edu

[1] Authors contributed equally

1. Introduction

For over a century thermoelectric devices have drawn little attention as a potential technology for terrestrial solar power conversion due to low efficiency and/or complicated and bulky designs, making the technology economically viable only for niche solar applications (Telkes, 1954; Goldsmid et al., 1980; Dent and Cobble, 1982; Rockendorf et al., 1999; Vatcharasathien et al., 2005; Li et al., 2010). Solar thermoelectric generators (STEGs) have also been designed and optimized for space applications due to their advantages of reliability and the capability to withstand high incident solar radiation (Fuschillo et al., 1966; Scherrer et al., 2003) However, constraints and designs for earth-based STEGs are different and have not been successfully optimized for large-scale and potentially cost-effective deployment on rooftops or for the integration in solar hot water systems. The most recent experimental work on STEG technology showed promising results for those types of applications (Kraemer et al., 2011).

The simplest design of a STEG consists of a unicouple thermoelectric generator (TEG) sandwiched between a solar absorber that absorbs the incident solar radiation and a heat sink that removes the excess heat to maintain the temperature difference across the unicouple TEG (Fig. 1). Typically a unicouple STEG includes optical components, such as a glass enclosure to maintain a vacuum and/or an optical concentrator system to increase the incident solar radiation on the absorber to reduce heat losses. The use of thermal concentration to focus absorbed solar radiation flux via lateral heat conduction within the absorber onto the thermoelectric generator has been proposed in several studies (Telkes, 1954; Fuschillo et al., 1966; Goldsmid et al., 1980; Rowe, 1981; Kraemer et al., 2011; Chen, 2011). The thermal concentration, C_{th}, is defined as the geometric ratio of the absorber surface area, A_{abs}, to the TEG cross-sectional area, A_{teg}. Just like optical concentration(Duffie and Beckman, 2006), the defined thermal concentration is not to be confused with the actual energy flux concentration which is also dependent on the properties and temperature of the solar absorber. Using thermal concentration reduces the amount of required thermoelectric material, and also increases the TEG efficiency by creating a higher absorber temperature. However, the thermal losses from the absorber become significant with increasing absorber temperature, suggesting the existence of an optimal op-

erational absorber temperature which balances the TEG efficiency gains with the radiation losses (Telkes, 1954; Rowe, 1981; Kraemer et al., 2011; Chen, 2011). A conceptual picture of the optimization of a STEG follows. A unicouple STEG comprises an optothermal system to convert radiation into a heat flux, and a unicouple TEG to convert the heat flux into electricity. The efficiency of a given optothermal system under given ambient conditions is a function of the temperature of the absorber, as material properties and radiation losses are a function of temperature. The efficiency of a unicouple TEG of given material properties and ambient conditions is also a function of the temperature of the absorber. Essentially, this absorber temperature is proportional to the product of the thermal resistance of the unicouple TEG, and the heat flow into it. The geometric parameter which determines the heat flow into the unicouple TEG is the absorber area; the geometric parameter which determines the thermal resistance of the unicouple TEG is the ratio (L/A_{teg}) where L is the length of the thermoelectric elements and A_{teg} is the cross-sectional area of the unicouple TEG. Therefore the geometric parameter which controls the absorber temperature, and thus the efficiency of a STEG, is the product $C_{th}L = A_{abs}(L/A_{teg})$. This simple, intuitive result was mathematically derived by Chen (2011) for a STEG with large thermal concentration, but only holds as long as certain conditions are met, which will be explained in this paper. Prior to the analysis by Chen (2011) a STEG design with large optical concentration was presented by Rowe (1981) based on similarly simplified models assuming constant thermoelectric and solar absorber material properties, geometry-independent radiative heat losses, no electrical contact resistance, and no thermal resistance in the solar absorber. Also, the inevitable variations of the incident solar radiation and cold-junction temperature of the STEG over the course of the day and the effect on the device optimization have not been addressed by previous publications.

In this paper we describe a STEG model accounting for various effects neglected by previous publications such as Rowe (1981), Chen (2011) and discuss in detail when and how those effects will influence the STEG performance and the STEG geometric optimization parameter. We show that only within certain limits the assumptions regarding contact resistance, thermal resistance, and geometry-dependent losses are valid. Simplifying the detailed model by introducing the justified simplifications allows to reduce the computational time significantly without losing accuracy. The model accounts for the temperature dependence of the thermoelectric materials and solar absorber properties while neglecting electrical contact resistances, the non-

uniformity of the absorber temperature, and the radiation exchange with the thermoelectric elements. Using this model we will discuss the influence of the inevitable variation of the solar intensity over the course of a day and the cold-junction temperature on the STEG performance and the STEG's geometric optimization parameter.

We also use this model to analyze the cogeneration application by integrating a STEG in a solar hot water system providing electricity and hot water. Even though this paper is mainly focused on STEGs with small or no optical concentration and large thermal concentration, the introduced optimization methodology and model can also be used for STEGs with large optical concentration.

2. General model

2.1. Geometry

The modeled STEG design as shown in Fig. 1(a) consists of a TEG unicouple (i.e. a pair of n- and p-type doped Bi_2Te_3 elements) sandwiched between a wavelength-selective solar absorber (Kennedy, 2002) and two polished copper electrodes, surrounded by a glass vacuum enclosure. The system can be placed in the focal point of an optical concentrator system to increase the operational temperature difference and conversion efficiency of the STEG (Kraemer et al., 2011). However, this work is mainly focused on non-optical concentrating STEGs with large thermal concentration. For the ease of the STEG fabrication the legs are of equal length but can have different cross-sectional areas. The solar absorber is a thin copper substrate coated with a wavelength-selective surface on the top side which absorbs the whole wavelength spectrum of the incident solar radiation. The copper substrate then conducts the heat laterally to the unicouple TEG which transports the concentrated heat to the cold junction while converting part of the heat into electricity. A heat sink removes the heat from the cold junction, where it is rejected to the surroundings or used for cogeneration.

2.2. Input parameters

Figure 1(b) shows the inputs into the various subsections of the model. The inputs to the optics model are the effective incident radiation on the plane of the aperture, $\dot{q}_{sol}$; the optical efficiency; and possible geometric optical concentration. The thermal model of the solar absorber requires the temperature-dependent emittance of the selective surface; the absorber

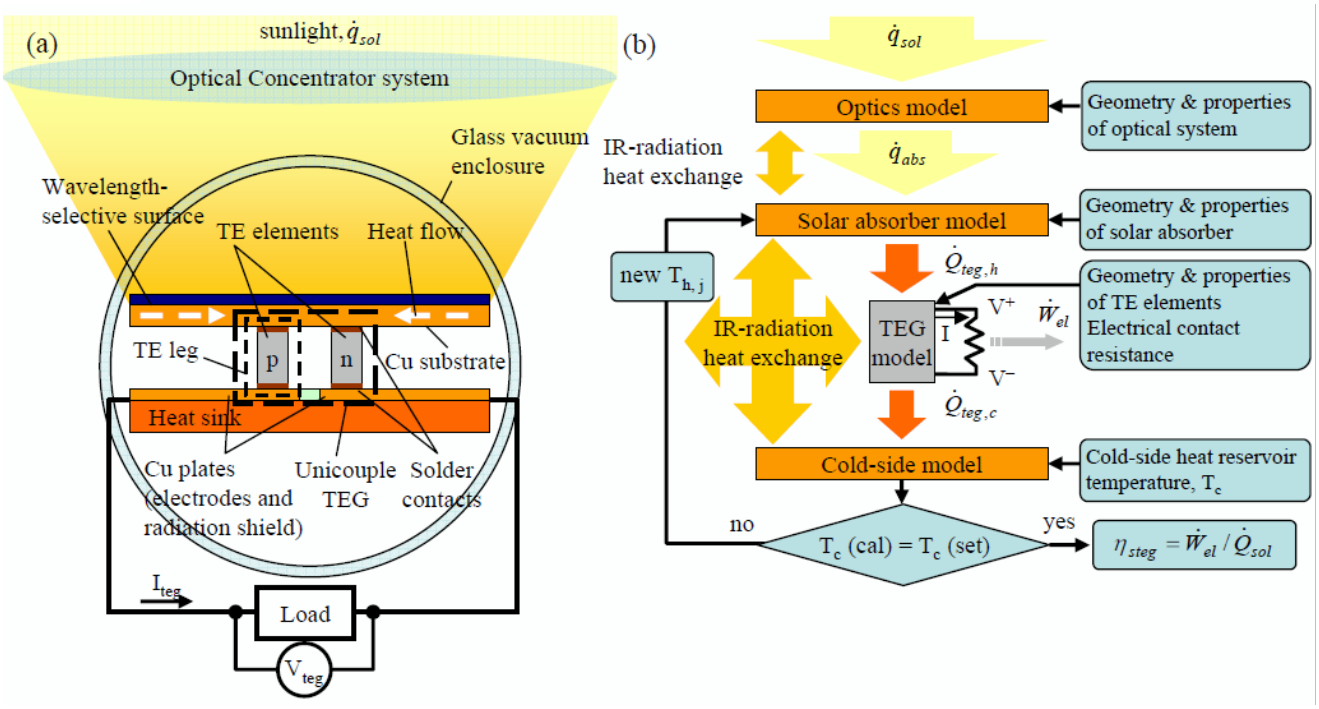

Figure 1: Concept of solar thermoelectric power conversion. (a) Schematic showing the concept of a solar-driven TEG cell consisting of a possible optical concentrator, a solar absorber (wavelength-selective surface on a copper substrate) which absorbs the solar radiation and thermally concentrates the heat onto the n/p-type unicouple TEG. The opposite side of the TEG is attached to copper electrodes that are used to connect the electrical circuit to extract the electrical power from the system; (b) Conceptual block diagram illustrating a solar thermoelectric generator (STEG) with its model components, the corresponding input parameter and the logic to calculate the heat flows and the electrical power output of the STEG.

geometry; and thermal conductivity of the absorber substrate. The TEG model requires the geometry of the different thermoelectric elements; the temperature-dependent thermoelectric material properties; the external electrical load; and the electrical contact resistance at the ends of the thermoelectric elements. The cold-side model requires the thermal conductance of the cold side. All four models also rely on the ambient temperature, and the geometry-related view factors between all the parts of the device. For the radiative heat balance of the back-side of the solar absorber with its surrounding (cold side, thermoelectric elements, gap between absorber and cold side) the emittance value of each participating surface must be know.

2.3. Governing equations

The STEG efficiency is defined as the ratio between the electrical power output, $\dot{W}_{el}$, and the incident solar radiation power, $\dot{Q}_{sol}$, which is the product of the effective incident solar radiation flux, $\dot{q}_{sol}$, and the aperture area, A_{ap}, of the STEG (Eq. 1)

$$\eta_{steg} = \frac{\dot{W}_{el}}{\dot{Q}_{sol}} = \frac{\dot{W}_{el}}{\dot{q}_{sol} A_{ap}} \tag{1}$$

$$J_{TIG} = \begin{cases} AT_E^2 e^{-\frac{\Phi_E}{kT_E}} - AT_C^2 e^{-\frac{\Phi_E - eV_{TIG}}{kT_C}} & \Phi_E > \Phi_C + eV_{TIG} \quad \text{Case A} \\ \mathrm{AT}_E^2 e^{-\frac{\Phi_E}{kT_E}} - AT_C^2 e^{-\frac{\Phi_C}{kT_C}} & \Phi_E = \Phi_C + eV_{TIG} \quad \text{Case B} \\ AT_E^2 e^{-\frac{\Phi_C + eV_{TIG}}{kT_E}} - AT_C^2 e^{-\frac{\Phi_C}{kT_C}} & \Phi_E < \Phi_C + eV_{TIG} \quad \text{Case C} \end{cases}$$

(2)

While the denominator of Eq. 1 is straightforward, the electric power must be calculated by using the submodels shown in Fig. 1(b). Without any simplifications, all four submodels must be solved simultaneously because of the radiation exchange between them. We will describe the submodels in detail below.

The optical model is a general model that lumps together the absorptance, α, of the solar absorber, the glass transmittance, τ, possible mirror reflection losses, the intercept factor, and the incident angle modifier to an

optical efficiency, $\eta_{opt} = \dot{Q}_{abs}/\dot{Q}_{sol}$ (Duffie and Beckman, 2006). This optical efficiency is defined as the ratio of the absorbed solar radiation to the solar radiation intercepted by the total aperture. In the following simulations the solar absorptance is assumed to be independent of temperature, which is a reasonable assumption for commercially available multilayer thin-film selective surfaces at temperatures below 250 °C. In the case of an optical-concentrating STEG system the optical concentration, C_{opt}, is the ratio of the aperture area to the absorber area, A_{abs}. The absorbed solar radiation heat flux can then be obtained from Eq. 3.

$$\dot{q}_{abs} = C_{opt}\eta_{opt}\dot{q}_{sol} \tag{3}$$

The optical performance of collectors such as the intercept factor and the incident angle modifier are specific to the optical design and beyond the scope of this work; more detailed discussions can be found in the literature (Duffie and Beckman, 2006). For the following simulation results the optical concentration, the intercept factor, and the incident angle modifier are set to 1.

The thermal model begins with the calculation of the temperature distribution within the solar absorber. A large lateral temperature drop within the absorber is not favorable for the system efficiency. The square-shaped solar absorber is approximated as a circular disk of equivalent surface area and is modeled as a radial fin with an absorbed radiation power, $\dot{Q}_{abs}$, distributed evenly over it as shown in Fig. 2(a). The closely-spaced thermoelectric elements are approximated as one cylindrical TEG with an equivalent cross-sectional area at a uniform hot-junction temperature. The largest radial temperature drop within the solar absorber occurs close to the unicouple TEG due to the large heat flux and thermal resistance. For the STEG design considered in this work with an absorber area much larger than the cross-sectional area of the thermoelectric elements it is reasonable to assume radial heat flow close to the unicouple TEG. Therefore the assumption of a circular solar absorber of equivalent area to estimate its temperature distribution is reasonable. The top side of the absorber has a temperature-dependent emittance, ϵ_{ss}. The back side of the absorber experiences radiative heat transfer with the cold side, the thermoelectric elements, and the environment through the gap between the absorber and the cold side. Within the absorber, the heat is conducted radially by the copper substrate of thickness t and thermal conductivity k_{abs}. The absorber is discretized radially. From the energy

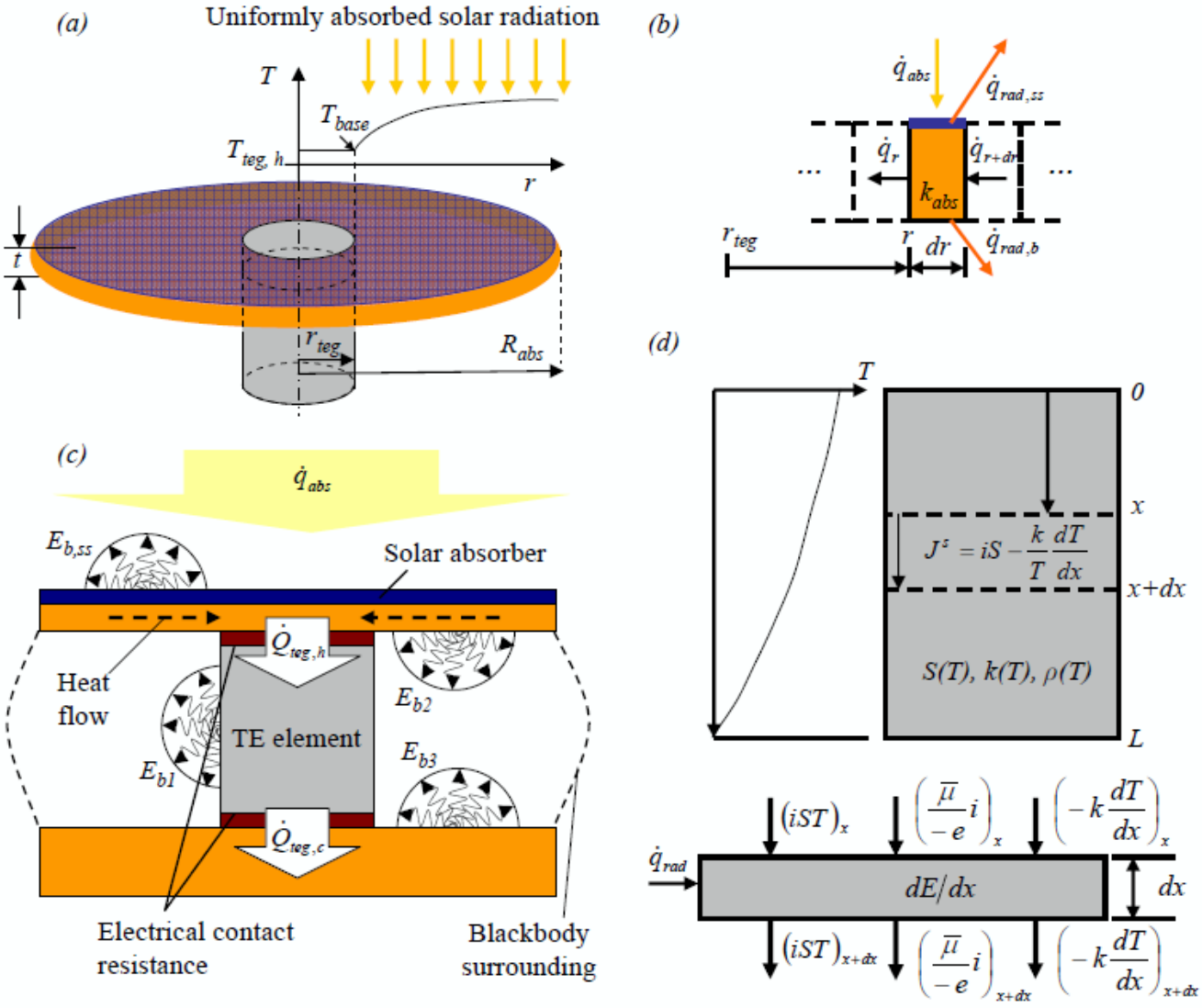

Figure 2: Schematics for STEG model. (a) Geometric model for STEG radiation calculations; (b) energy balance over an absorber segment for the radially discretized solar absorber; (c) 2D Schematic of a STEG showing the merged unicouple thermoelectric generator (TEG) with radiative heat losses; $E_{b,ss}$, E_{b1}, E_{b2}, and E_{b3} are emissive powers of the surfaces; $\dot{Q}_{teg,h}$ and $\dot{Q}_{teg,c}$ is the heat absorbed at the hot junction and rejected at the cold junction; (d) 1D discretization of a thermoelectric element and energy balance of a segment for iterative numerical calculations.

balance over one elemental ring of the absorber (Fig. 2(b)) Eq. 4 is obtained which then can be solved for the temperature non-uniformities within the solar absorber (Fig. 2(a)) using a finite difference scheme.

$$\frac{dT_{abs}}{dr} + r\frac{d^2T_{abs}}{dr^2} = \frac{(2r+dr)}{2k_{abs}t}\left[\dot{q}_{abs} - \epsilon_{ss}\left(T(r)\right)\sigma\left(T_{abs}^4 - T_\infty^4\right) - \dot{q}_{rad,b}\right] \quad (4)$$

The first term in the brackets represents the absorbed incident solar radiation; the second term accounts for the net radiative heat flux from the selective surface of the solar absorber at a temperature $T_{abs}(R)$ to the glass enclosure treated as a blackbody surface at ambient temperature T_∞; the third term represents the net radiative heat flux from the back side of the solar absorber, $\dot{q}_{rad,b}$. The net radiative heat flux couples the thermal absorber model, the TEG model, and the cold-side model as shown in Fig. 1(b) and Fig. 2(c), and is described with the thermoelectric model below. Equation 4 is solved numerically with the hot-junction temperature as the boundary condition at the base of the fin, $T\left(r = r_{teg}\right) = T_{base} = T_{teg,h}$ and with the absorber edge radiation flux, $\dot{q}_{rad,e} = \epsilon_{cu}\sigma\left(T_{abs}^4\left(r = R_{abs}\right) - T_\infty^4\right)$, as a Neumann boundary condition for the absorber with radius, R_{abs}. The emittance of the polished copper substrate, ϵ_{cu}, is assumed to be 0.03 (Mills, 1999). The absorber is assumed to be at a uniform hot-junction temperature in the region ($r < r_{teg}$) where the absorber is thermally attached to the TEG. This is a necessary assumption for the later-introduced 1D discretization model of the thermoelectric elements. A detailed discussion in section 3.3 will justify this assumption for STEG designs optimized according to the methodology proposed by this paper. In other STEG designs this assumption might not be valid and will lead to an overestimation of the STEG performance. The temperature distribution of the absorber is determined and the heat flux at the hot-junction of the TEG can be obtained from Eq. 5.

$$\dot{q}_{teg,h} = \left[\dot{q}_{abs} - \frac{\sigma}{A_{abs}}\iint_{A_{abs}} \epsilon_{ss}\left(T_{abs}(r)\right)\left(T_{abs}^4(r) - T_\infty\right)dA - \frac{\dot{Q}_{rad,b} + \dot{Q}_{rad,e}}{A_{abs}}\right] C_{th} \quad (5)$$

The heat flux into the TEG becomes the boundary condition for the TEG model. The first term in the brackets is the absorbed radiation heat flux, the second term is the integrated net radiative heat loss from the wavelength-selective surface to the blackbody surroundings, and the third term consists

of the net thermal radiation heat flow from the copper back side, $\dot{Q}_{rad,b} = (A_{abs} - A_{teg})\,\dot{q}_{rad,b}$, and from the edges, $\dot{Q}_{rad,e} = (2\pi R_{abs} t)\,\dot{q}_{rad,e}$, of the solar absorber. The edge heat losses can be minimized by choosing a thin copper substrate. However, reducing the thickness of the copper substrate increases the radial thermal resistance and will result in larger radial temperature gradients within the absorber.

The TEG model is a discretized model of the thermoelectric elements which incorporates thermoelectric effects as well as contact resistance, radiation exchange of the legs with the surroundings, and the external electrical load. The model, shown in Fig. 2(d), is described in Eq. 6.

$$\frac{1}{A_{leg}}\frac{dE}{dx} = \frac{\mathcal{P}_{leg}\dot{q}_{rad}(x)}{A_{leg}} = \frac{\partial(iST)}{\partial x} - \frac{1}{e}\frac{\partial(\bar{\mu}i)}{\partial x} - \frac{\partial}{\partial x}\left(k(x)\frac{\partial T}{\partial x}\right) \tag{6}$$

This differential equation is a one-dimensional energy flux balance over a segment of a discretized thermoelectric element at position x, where the left hand side represents the change in total energy dE in the segment of length dx divided by the cross-sectional area, A_{leg}, of the thermoelectric element. This change in energy dE/dx is equal to the net radiative heat flux, $\dot{q}_{rad}$, to the thermoelectric element segment at position x from its surroundings multiplied by the leg equivalent perimeter, $\mathcal{P}_{leg}$, of the thermoelectric element. A detailed multi-body radiative heat transfer model with the emissive powers $E_{b,ss}$, $E_{b,1}$, $E_{b,2}$, and $E_{b,3}$ of each contributing surface as shown in Fig. 2(c) determines the radiative heat loss from the unicouple STEG, including the radiation from the edges of the solar absorber and from the thermoelectric elements. In the model the two thermoelectric elements are merged to one cylindrical thermoelectric element with an equivalent surface area $A_{s,eq} = 3L\left(\sqrt{A_p} + \sqrt{A_n}\right)$ to simplify the view factor calculations (Modest, 2003) where A_p and A_n are the cross-sectional areas of the p- and n-type thermoelectric elements. The equivalent surface area is based on the assumption that the net radiative heat transfer from the side walls of the thermoelectric elements facing each other is negligible because the closely spaced n- and p-type thermoelectric elements have similar temperature profiles. Consequently, the facing side walls mainly radiate to one another at similar temperatures, which reduces the net radiative heat transfer significantly. Therefore the facing side walls act as radiation shields for one another. The corresponding effective leg perimeter is $\mathcal{P}_{leg} = 3\sqrt{A_{leg}}$. The thermoelectric elements are closely spaced in order to obtain mechanically-

reliable unicouple STEGs with stable electrical and thermal contacts. The thermoelectric elements are soldered to the solar absorber which expands and contracts due to thermal cycling during operation. Consequently, the thermal expansion/contraction will apply shear stresses on the solder joints. The larger the distance between the thermoelectric elements the larger would be the displacement and thus the shear stresses that cause the degradation of the contacts and ultimately the failure of the joints.

The thermoelectric elements are discretized in small isothermal sections and the view factors can be determined with view factor algebra (Modest, 2003) by approximating the square-shaped absorber and cold side as two finite disks at uniform temperature of equivalent surface area with radius R_{abs} (Fig. 2(a)). In order to take into account the increase in radiation losses from the solar absorber back side due to the possible non-uniformity of its temperature, the temperature is averaged over the equivalent radius of the absorber. After all view factors are determined the net radiative heat flux from each surface can be obtained with the net radiation method (Modest, 2003). The emittance of the back side and edges of the solar absorber (polished copper), and the cold side (polished copper) is assumed to be temperature independent with $\epsilon_{cu} = 0.03$ (Mills, 1999). The emittance of the thermoelectric elements is assumed to be constant with $\epsilon_{te} = 0.5$. For more accurate performance predictions of an unicouple STEG with long thermoelectric elements the temperature dependence of the emittance should be included. However, for a high-performance and cost-effective STEG design with large thermal concentration and short thermoelectric elements the accurate knowledge of their radiative properties is not important as the analysis will show. The first term on the right hand side of Eq. 6 represents the change in heat flux related to the entropy carried by the electrical current flux, i. The second term is the change in energy flux due to the change in the electrochemical potential, $\nabla\overline{\mu}$, of the energy carriers divided by the electron charge $(-e)$: $1/(-e)\,\nabla\overline{\mu} = -S\nabla T - \rho i$, where S is the temperature-dependent Seebeck coefficient of the material, and ρ is the electrical resistivity. This equality can be derived from the theory of irreversible thermodynamics and is referred to as the generalized Ohm's law (Domenicali, 1953). The third term is the change in the conducted heat with the thermal conductivity $k(x)$. An equation for the local thermoelectric heat flux can be obtained from the entropy flux $J^s(x) = iS(x) - \frac{k(x)}{T(x)}\frac{dT}{dx}$ at position x inside the thermoelectric element. The Seebeck coefficient $S(x)$ is defined as the entropy carried per

electron charge (Domenicali, 1953). Multiplying the entropy flux by the local temperature yields the local thermoelectric heat flux.

$$\dot{q}_{leg}(x) = i\,(ST)_x - \left(k\frac{dT}{dx}\right)_x \tag{7}$$

The differential equations Eq. 6 and Eq. 7 can be arranged into a coupled set of first-order equations (Mahan, 1991; Hogan and Shih, 2006) and are shown below, including the net thermal radiative heat transfer of the thermoelectric element side walls.

$$\frac{dT}{dx} = \frac{i\,(ST)_x - \dot{q}_{leg}(x)}{k(x)} \tag{8}$$

$$\frac{d\dot{q}_{leg}}{dx} = \left[i\rho(x) + S(x)\,\frac{i\,(ST)_x - \dot{q}_{leg}(x)}{k(x)}\right] i - \frac{3\dot{q}_{rad}(x)}{\sqrt{A_{leg}}} \tag{9}$$

Those coupled first-order equations are solved iteratively (Hogan and Shih, 2006; Buist, 1995) for the n- and p-type element (with known temperature-dependent properties) for the optimal thermoelectric heat flux and temperature distribution corresponding to the optimum current densities for a specified TEG geometry (lengths and cross-sectional areas of thermoelectric elements). The thermoelectric elements are chosen to have the same length. Due to the difference in the n- and p-type thermoelectric material properties, the cross-sectional area of the thermoelectric elements are different and the cross-sectional area ratio must be optimized during the iteration process. The boundary conditions for the differential equations of both thermoelectric elements are the same fixed cold- and hot-junction temperatures that uniquely determine the optimal current, the temperature and heat flux distribution for the specified unicouple TEG geometry. Electrical contact resistances are included in the calculations by adding a small segment with corresponding electrical resistivity and zero Seebeck coefficient to the hot and cold end of the thermoelectric elements. From the determined energy flows entering and leaving the TEG, the electrical power output of the STEG is found with the following equation.

$$\dot{W}_{el} = A_{teg}\dot{q}_{teg,h} - \left\{\dot{Q}_{teg,n} + \dot{Q}_{teg,p}\right\}_{x=L} + \mathcal{P}_{teg}\int_0^L \dot{q}_{rad}(x)\;dx \tag{10}$$

The first term on the right-hand side of Eq. 10 is the TEG heat flux at the hot junction, $\dot{q}_{teg,h}$, which is the heat flux absorbed and concentrated by

the solar absorber. The term in braces is the heat rejected, $\dot{Q}_{teg,c}$, at the cold junction ($x = L$) by the n- and p-type thermoelectric elements. The last term is the net radiative heat transfer of the TEG with its surroundings with $P_{teg} = 3(sqrtA_p + sqrtA_n)$ as the Perimeter and $\dot{q}_{rad}(x)$ as the net radiative heat flux of the unicouple TEG. The excess heat, $\dot{Q}_{excess}$, that must be removed on the cold side to maintain the optimal temperature difference across the TEG can then be defined with Eq. 11.

$$\dot{Q}_{excess} = \dot{Q}_{teg,c} + \dot{Q}_{rad,c} = U\,(T_{c,j} - T_c) \tag{11}$$

The cold side is modeled as a heat sink to the ambient or to a working fluid with an overall heat transfer coefficient (HTC), U, which is assumed to be infinitely large for some simulations to simplify the calculations by using a cold-junction temperature, $T_{c,j}$, which is equal to the fixed cold-side temperature, T_c. The net radiative heat transfer, $\dot{Q}_{rad,c}$, between the cold side and the other parts of the system is calculated from the aforementioned radiation model.

2.4. Optimization for fixed incident radiation flux

With the introduced models the geometry of the unicouple STEG (Fig. 1(a)) must be optimized for optimal hot-junction temperature which yields highest electric power output (Eq. 10) and corresponding highest STEG efficiency as discussed in the introduction. The geometrical optimization is performed for a constant incident solar radiation flux and a fixed cold-side temperature. Furthermore, some constraints are enforced on the optimization. The length and the current of both thermoelectric elements are the same. Additionally, the cold-junction and hot-junction temperatures of both thermoelectric legs are set to be equal. The temperature and the heat flow at the hot junction are introduced as matching boundary conditions for the solar absorber and the hot junction of the unicouple TEG. Under those constraints all dimensions of the unicouple STEG (length and cross-sectional areas of thermoelectric elements, and the absorber size) are varied, and load matching for each set of geometries is performed to find the optimal geometry.

3. Discussion

The performance of a STEG is negatively affected by contact resistance losses, the temperature non-uniformity of the absorber, the radiation losses

out the gap between the absorber and cold side, and the radiation losses from the sidewalls of the TEG. These four loss mechanisms are all geometry-dependent, and are included in the introduced detailed model. However, those losses can be minimized if the system geometry meets certain constraints. In the first part of this section, the necessary constraints for each of these loss mechanisms are developed. When the STEG design meets these constraints, the STEG can be modeled in a much simpler manner. In the second part of this section a STEG optimization methodology based on this simplified model is introduced and discussed. For all simulations the STEG comprises an evacuated glass tube with an effective transmittance of 90.5%; a commercial wavelength-selective solar absorber with known temperature-dependent properties, a copper substrate thermal conductivity of 380 W/mK, and a thickness of 0.2 mm; nanostructured Bi_2Te_3 compound thermoelectric materials, as described by Poudel et al. (2008); AM1.5G (ASTM, 2008) solar flux striking the glass tube; and an ambient and cold-junction temperature of 25 °C unless stated differently.

3.1. Effect of electrical contact resistance

In order to obtain the best performance of a STEG, the relative electrical contact resistance must be minimized. To gauge how the geometry affects the contact resistance losses, the other geometry-dependent losses are turned off in the simulation. This is accomplished in three steps: giving the absorber infinite thermal conductivity eliminates temperature gradients in the absorber; setting to zero the emittance of the thermoelectric elements eliminates radiation losses from the thermoelectric elements; and setting to 1 the view factor from the absorber to the cold side (the infinite parallel plate assumption) prevents the absorber backside losses from being geometry-dependent. Figure 3(a) shows the effect of different electrical contact resistances on the efficiency of a unicouple STEG under these conditions. These assumptions yield an upper limit for the STEG efficiency of 5.1%. The results show that the reduction of the STEG efficiency due to electrical contact resistance becomes larger with decreasing thermoelectric element length, which has been pointed out before for other thermoelectric devices (Goldsmid, 1986). The minimum electrical contact resistance for a Bi(Sb)-Te/metal interface is estimated to be on the order of $10^{-11}\,\Omega\text{cm}^2$ (da Silva and Kaviany, 2004). Gupta et al. (2010) experimentally demonstrated electrical contact resistances below $10^{-7}\,\Omega\text{cm}^2$ for Bi_2Te_3 sputter-coated with Ni or Co. As shown in Fig. 3(a), if the electrical contact resistance is as small as $10^{-7}\,\Omega\text{cm}^2$ the effect

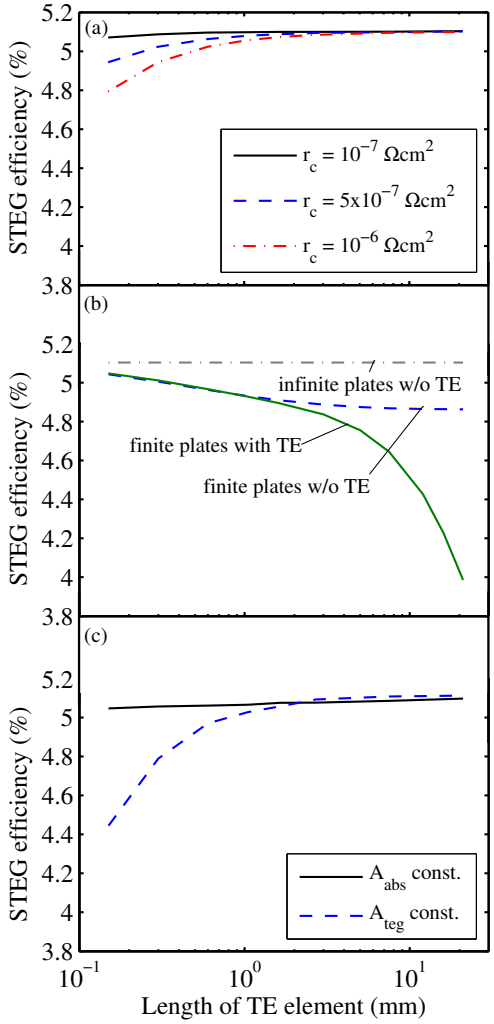

Figure 3: The effect of the system losses of a simple flat-plate unicouple STEG geometry on the STEG performance. (a) Effect of the electrical contact resistance r_c: $10^{-7}\,\Omega\text{cm}^2$ solid line, $5\text{x}10^{-7}\,\Omega\text{cm}^2$ dashed line, $10^{-6}\,\Omega\text{cm}^2$ dash-dotted line; (b) Effect of geometry-dependent radiative heat losses for a unicouple STEG with constant finite parallel plates (absorber size of $911\,\text{mm}^2$ including (solid line) and excluding (dashed line) thermoelectric element radiation losses compared to a unicouple STEG assuming infinite parallel plates excluding the thermoelectric elements from the heat balance (dash-dot line); the cross-sectional of the unicouple TEG is altered to find optimum Cth_L; (c) Effect of the non-uniformity of solar absorber temperature; for each length of the thermoelectric element the optimal $C_{th}L$ is found in one case by varying the cross-sectional area of the TEG (A_{teg}) while keeping the absorber area (A_{abs}) constant ($911\,\text{mm}^2$) in the other case by changing A_{abs} while keeping A_{teg} constant ($3.645\,\text{mm}^2$).

on the STEG performance is negligible even for thermoelectric elements as short as 0.1 mm. Other plating processes can result in higher electrical contact resistances which then cannot be neglected in the design optimization and will limit the minimum value of the thermoelectric element length.

3.2. Geometry-dependent radiation losses

In a STEG cell design as shown in Fig. 1(b), the STEG geometry affects the radiation exchange between the TEG, the cold side, the back side of the absorber, and the environment. Ideally the sidewalls of the TEG would not contribute to the radiative heat balance, and the absorber and cold side would be infinite parallel plates where no radiation from the back side of the absorber escapes through the gap to the environment. This limit is shown in the dash-dotted line in Fig. 3(b). The dashed line in Fig. 3(b) shows the effect of the geometry-dependent radiation losses resulting from a finite size of the parallel plates on the performance of the unicouple STEG, excluding the radiation losses from the thermoelectric elements. The solid line shows the effect of both geometry-dependent radiation losses. For these calculations the electrical contact resistance is set to zero and the absorber is assumed to have infinite thermal conductivity. The absorber size is set to 911 mm^2, and the TEG cross-sectional area, A_{teg}, is varied to find the optimal thermal concentration at each thermoelectric element length. The results show that excluding the geometry dependence of the radiative heat losses from the unicouple STEG can lead to an overestimation of its efficiency, especially for a STEG with longer thermoelectric elements when the radiation contributions of the elements become significant. The contribution of the radiative heat loss from the thermoelectric elements is very small for thermoelectric elements shorter than 4 mm which permits to ignore them in the radiative heat transfer model and thus tremendously reduce the computational time. Additionally, this observation is the necessary justification for the separation of the TEG efficiency from the rest of the system (Fig. 1(a)) as suggested in this paper and was assumed to be valid by several other authors (Telkes, 1954; Rowe, 1981; Chen, 2011). With further reduction of the thermoelectric element length the unicouple STEG efficiency asymptotically approaches the efficiency value of 5.1% of a STEG with infinite parallel plates. In conclusion, the radiation loss contribution of the gap, and with that the variation of the radiative heat loss from a unicouple STEG as a function of thermoelectric element length, must be included in order to make accurate predictions of its performance. For example, increasing the length of the unicouple TEG from

0.1 mm to 3 mm will reduce the STEG efficiency by approximately 6%rel (Fig. 3(b). However, assuming that in a final STEG design several unicouple STEGs are closely-placed next to each other, this effect on the STEG efficiency is significantly reduced.

3.3. Temperature non-uniformity in the solar absorber

Choosing short thermoelectric elements results in minimal material use while also maximizing the potential unicouple STEG efficiency (if electrical contact resistance can be ignored) by minimizing radiative heat losses. However, short thermoelectric elements require large heat fluxes and thus a large thermal concentration to maintain a large temperature difference. This large thermal concentration can result in a large radial temperature drop within the solar absorber from its outer edge to the thermoelectric elements as briefly discussed in section 2 (Fig. 2(a)).

If the temperature non-uniformity in the solar absorber is large, then most of the absorber will have a significantly higher temperature than its junction with the thermoelectric elements, resulting in higher radiative heat losses than if the absorber temperature were uniform at the hot-junction temperature. This penalizes the thermal efficiency and thus the heat flux concentration. Figures 4 and 5 show the temperature distribution in the solar absorber for various thermal concentrations. In Fig. 4(a) the thermal concentration is changed by varying the absorber size while keeping the thermoelectric element cross-sectional area the same (equivalent radius $r_{teg} = 1.08\,\mathrm{mm}$). In Fig. 4(b) the solar absorber size is kept constant (equivalent radius $R_{abs} = 17.03\,\mathrm{mm}$) while the cross-sectional area of the thermoelectric elements is varied. The temperature drop within the absorber in the latter case is significantly smaller than in the case with constant thermoelectric cross-sectional area and changing absorber size. This is because the heat flux conducted radially is proportional to the square of the absorber radius, but the increase of the radial conduction resistance scales with $ln\,(R_{abs}/r_{teg})$ (Mills, 1999). Therefore it is best to adjust the thermal concentration via a decrease in cross-sectional area to keep the temperature drop within the absorber as small as possible. Figure 4(c) shows simulation results using a significantly larger cross-sectional area of the thermoelectric elements, which could represent a TEG module with a large number of closely packed thermocouples. The simulations show that with an equivalent thermoelectric element radius of 4.8 mm (corresponding to 20 thermocouples with equivalent radius of 1.08 mm each), the temperature drop within the absorber

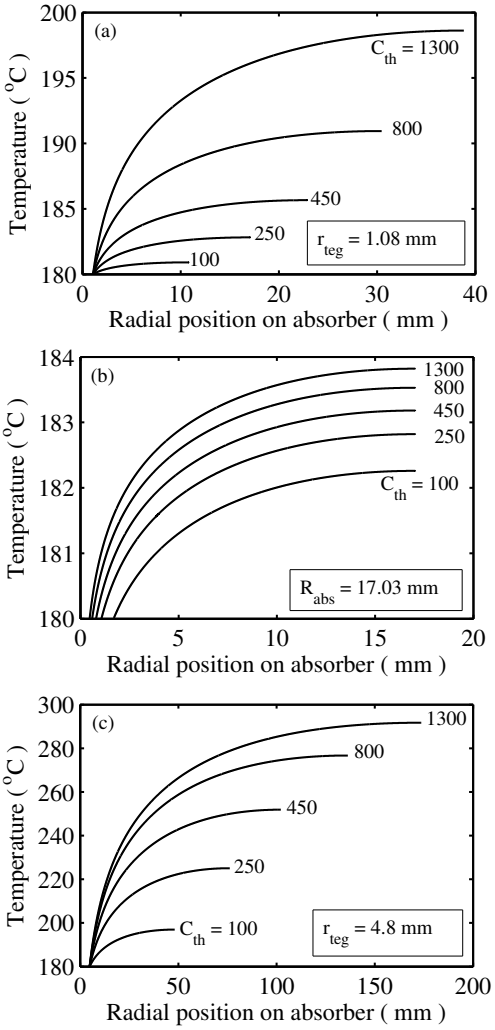

Figure 4: Non-uniformity of the solar absorber temperature obtained from a radial finite-difference scheme. Solar absorber substrate is copper ($k = 380\,\mathrm{W/mK}$) of thickness $t = 0.2\,\mathrm{mm}$. Simulation results for various thermal concentrations, $C_{th} = \frac{A_{abs}}{A_{teg}}$ with (a) fixed thermoelectric element radius (r_{teg}), (b) fixed absorber radius (R_{abs}), and (c) large r_{teg} (fixed) equivalent to 20 closely-packed thermoelectric unicouples.

becomes very large in order to support the large heat flux.

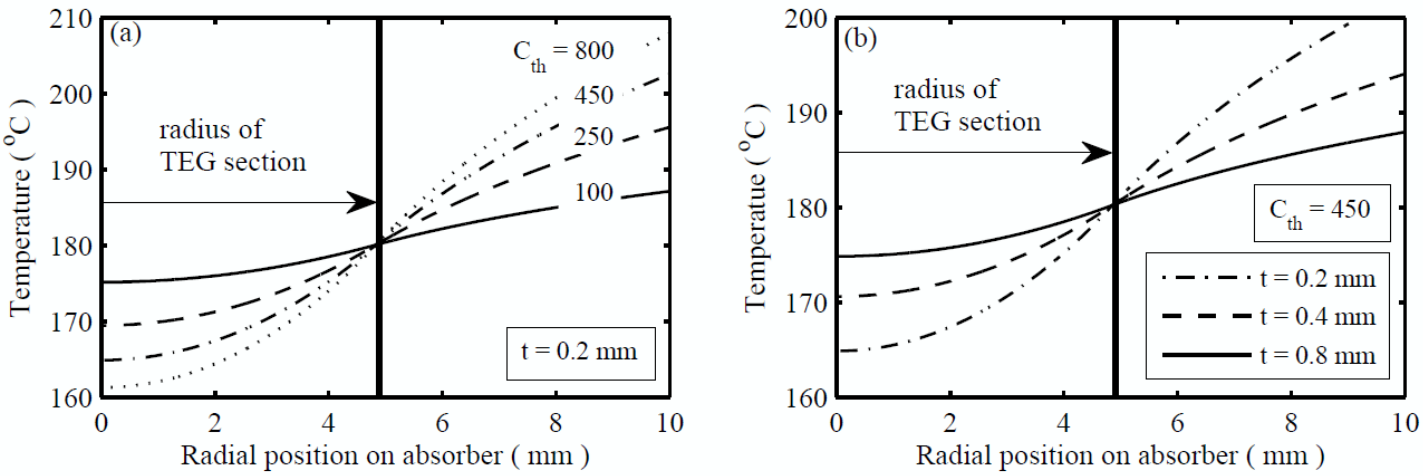

Figure 5: Temperature distribution within the solar absorber in the TEG section with radius r_{teg} of 4.8 mm, (a) for absorber thickness $t = 0.2\,\text{mm}$ and different thermal concentration C_{th} and (b) for $C_{th} = 450$ and different solar absorber thicknesses.

In addition to the temperature gradient away from the TEG module, there will also be a significant temperature non-uniformity over the TEG module, as shown in Fig. 5, if a large number of thermoelectric elements are closely packed and if due to cost considerations the copper substrate thickness t is chosen to be small (e.g., 0.2 mm). However, comparing figures 4(c) and 5(a), the temperature drop in the TEG junction region is ≈ 5 times smaller than in the absorber region away from the TEG. This can be explained from the rapid decrease of the radial heat flux within the solar absorber due to the heat removed by the TEG. However, in not carefully designed STEGs this non-uniformity of the absorber temperature forces a large portion of the TEG to operate at off-optimal hot-junction temperatures which leads to a reduction in the STEG efficiency. The above concerns suggest that conventional TEG modules with a large number of closely spaced thermoelectric elements are less suitable for solar applications with large thermal concentration. The best performance will be achieved for unicouple STEGs that individually consist of solar absorbers mounted to small thermoelectric unicouples with small cross-sectional areas as shown in Fig. 1(a). For all simulated cases up to a thermal concentration of 1300 the expected radial temperature increase within the solar absorber away from the unicouple TEG is less than 4 °C.

The temperature drop within the unicouple TEG region can be estimated to be significantly smaller than 1 °C. Consequently, it is reasonable to assume a uniform absorber temperature equal to the hot-junction temperature of the thermoelectric unicouple. Figure 3(c) shows the effect of the temperature non-uniformity of the solar absorber on the maximum unicouple STEG efficiency. The two curves show the difference between optimizing the thermal concentration by changing A_{teg} versus by changing A_{abs} and fixing A_{teg}. The effect on the efficiency as a function of chosen element length, L, is significantly larger for the case with a constant cross-sectional area of the thermoelectric elements. This confirms that if the element length is to be reduced in order to minimize material cost without significantly affecting the uniouple STEG performance, a smaller cross-sectional area of the thermoelectric elements must be chosen to increase C_{th}.

3.4. Simplified STEG model

If the contact resistance, the temperature non-uniformity of the absorber, the radiation losses from the leg, and the geometry dependence of the view factors can be ignored, then the STEG model becomes much simpler for three reasons. First, the absorber efficiency is independent of geometry. Second, the discretized TEG submodel can be solved independently of the absorber model as long as the temperature and heat flux at the junction are matched. Third, once a maximum efficiency has been found for given ambient conditions, the system geometry can be scaled without affecting the efficiency as long as four parameters - C_{opt}, $C_{th}L$, the length-weighted current iL, and the ratio of thermoelectric leg cross-sectional areas A_n/A_p - are held constant. To show this independence of individual unicouple STEG geometries, the efficiency with the above simplifying assumptions can be expressed as

$$\eta_{steg} = \frac{\dot{q}_{abs} - \dot{q}_{rad,ss} - \dot{q}_{b,app}}{C_{opt}\dot{q}_{sol}} \left(1 - \frac{\Phi_{c,p} + \Phi_{c,n}}{\left(\frac{D_p}{i_p L} + \frac{D_n}{i_n L}\right) \left[\dot{q}_{abs} - \dot{q}_{rad,ss} - \dot{q}_{b,app}\right] (C_{th} L)} \right) \tag{12}$$

$$D_p = \left(1 + \frac{A_n}{A_p}\right) \left(\frac{1}{1 + A_{abs,n}/A_{abs,p}}\right) \tag{13}$$

$$D_n = \left(1 + \frac{A_p}{A_n}\right) \left(\frac{1}{1 + A_{abs,p}/A_{abs,n}}\right) \tag{14}$$

The term in front of the parentheses in Eq. 12 is the optothermal efficiency of the unicouple STEG which is often split into an optical and thermal concentrating collector efficiency (Rowe, 1981; Duffie and Beckman, 2006; Kraemer et al., 2011; Chen, 2011). It is the fraction of the intercepted solar radiation power which is delivered to the TEG. The heat loss is determined by the net radiative heat transfer, $\dot{q}_{rad,ss}$, from the selective surface to the blackbody surroundings (section 2) and by the net radiative heat loss from the back side of the solar absorber, $\dot{q}_{b,app} = \epsilon_{eff}\sigma\left(T_{abs}^4 - T_\infty^4\right)$ with ϵ_{eff} as the effective emittance which is assumed to be independent of the thermoelectric element length. As discussed in section 3.2, this assumption introduces the largest error to the model, however, the inaccuracy is significantly reduced if a STEG with a large number of closely-spaced unicouple STEGs is considered.

The second factor of the STEG efficiency is the TEG efficiency derived from thermoelectric potentials, $\Phi = 1/u + ST$, with the relative current density $u = i/\left(-k\nabla T\right)$ defined as the ratio of the electrical current density to the conducted heat flux (Snyder and Ursell, 2003). The model can be further simplified by using the TEG efficiency equation based on the averaged $(ZT)_{avg}$ (Ioffe, 1957) if the thermoelectric leg is self-compatible (Snyder and Ursell, 2003). However, the following results include the temperature dependence of the thermoelectric material properties via the previously described numerical model (section 2). Chen (2011) showed mathematically that $C_{th}L$, the product of the thermal concentration and the length of the thermoelectric elements, is the optimization parameter of a STEG if the thermoelectric material properties are constant amongst other assumptions. However, assuming constant material properties for the thermoelectric elements and the solar absorber can lead to unrealistic results, significantly over-predicting the conversion efficiency of a STEG (Chen, 1996). Equation 12, which holds for temperature-dependent material properties, shows that the efficiency is not dependent on individual dimensions of the unicouple STEG but is determined by the single geometric optimization parameter, $C_{th}L$ as long as the optical efficiency and optical concentration does not change. If the thermoelectric elements exhibit a difference in their properties of n- and p-type materials, the ratios of the thermoelectric element cross-sectional areas, A_p and A_n, and of the corresponding absorber sections, $A_{abs,p}$ and $A_{abs,n}$, that set the heat input into the individual n- and p-type unicouple STEG sections (Eq. 13 and 14) deviate from 1 and are uniquely defined for the point of maximum efficiency at a specific $C_{th}L$. Furthermore, the optimum length-weighted electrical cur-

rent densities, i_pL and i_nL, are uniquely defined through the same $C_{th}L$. The relative current densities and with that the thermoelectric potentials at the cold junction are determined by the length-weighted electrical current densities and therefore are indirectly only dependent on $C_{th}L$. In summary, there is an optimal $C_{th}L$ that yields maximum unicouple STEG efficiency with corresponding area ratios, length-weighted electrical current densities and thermoelectric potentials if the STEG is designed in such a way that the necessary assumptions discussed in this paper hold. This permits the length and cross-sectional area of the TEG as well as the area of the solar absorber to be chosen arbitrarily within the established limits without affecting the STEG performance as long as the optimized $C_{th}L$, length-weighted electrical current densities and the area ratios (Eq. 13 and 14) yielding maximum efficiency are unaltered. Consequently, it is possible to reduce the volume of the thermoelectric elements and with that the thermoelectric material cost for a fixed size of solar absorber.

4. Applications

4.1. Rooftop STG performance

So far we have discussed the dependence of the optimal geometric parameter, $C_{th}L$, on the individual dimensions of the STEG for fixed cold-junction temperature and incident solar radiation. In reality those parameters are not constant over the course of a day or a year and are location specific. The STEG performance (Kraemer et al., 2011) is affected by the incident solar radiation flux and cold-junction temperature and so will be the optimal geometric parameter, $C_{th}L$.

A STEG is optimized in this section for earth-based electricity production and its performance is predicted using the developed model neglecting electrical contact resistances, assuming a uniform solar absorber temperature equal to the hot junction temperature, and ignoring the thermoelectric elements in the radiative heat balance. The solar absorber is chosen to be 50 mm wide and of infinite length (for view factor calculations); Each thermoelectric element is 1.6 mm long, and the total cross-sectional area of one unicouple TEG is 3.645 mm^2.

The thermoelectric efficiency of the STEG is strongly affected by the amount of current that flows through the electrical circuit. Figure 6(a) shows the calculated output voltage and efficiency as a function of the current (up to the short-circuit current) for a STEG with $C_{th}L = 0.4\,\text{m}$ with a cold-junction

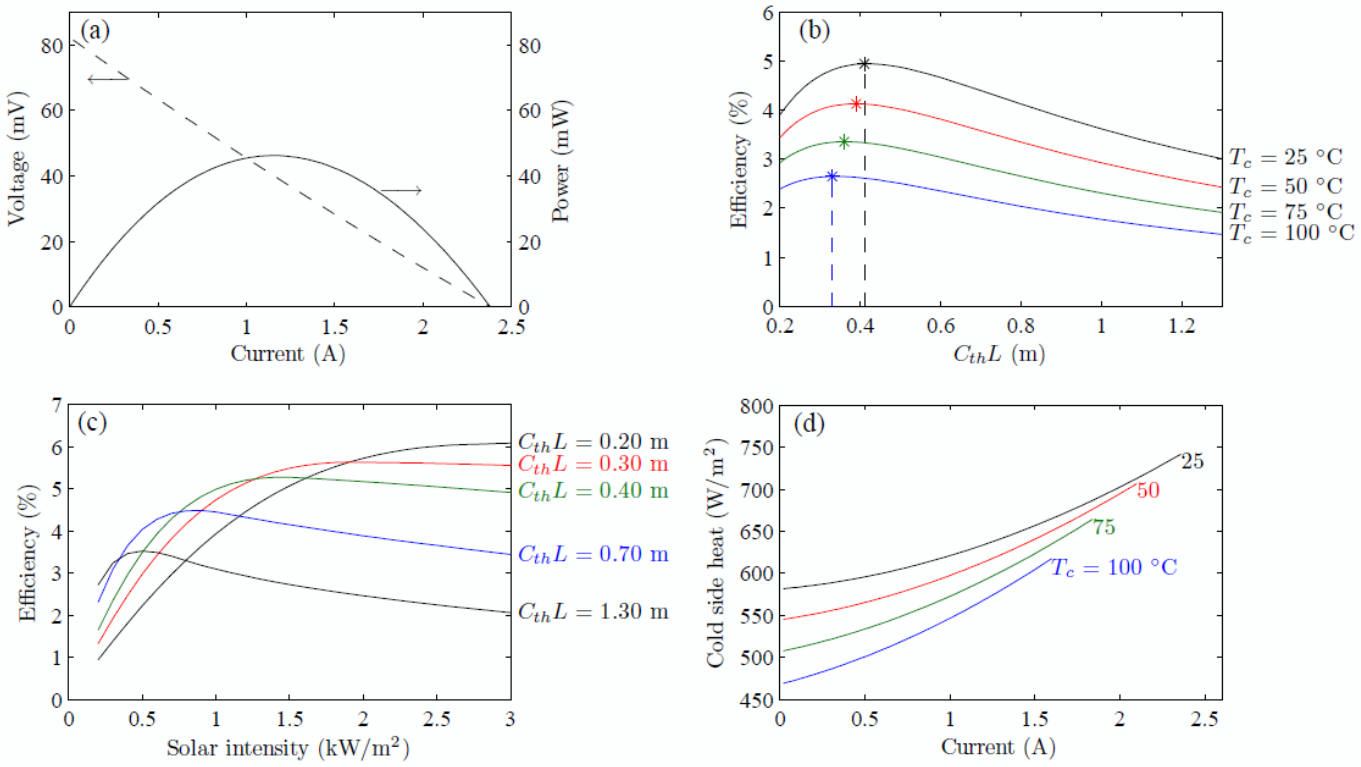

Figure 6: STEG performance characteristic. (a) Voltage and power output as a function of current for an optimized unicouple STEG ($C_{th}L$ = 0.4 m) under 1 kW/m^2 illumination, cold-junction temperature of 25 °C, and chosen thermoelectric element dimensions (WxDxL) of 1.35 mmx1.35 mmx1.6 mm; Simulation results for a STEG of 1 m^2 area. (b) STEG efficiency as a function of the geometric parameter $C_{th}L$ for different cold-junction temperatures; (c) STEG efficiency as a function of incident solar intensity for different $C_{th}L$; (d) excess heat released at the cold side for various cold-junction temperatures as a function of the STEG current.

temperature of 25 °C. The I-V curve clearly shows a series-resistance limited behavior of the STEG cell which is not due to resistances at the electrical contacts or in the electrical circuit but due to the high resistivity of Bi_2Te_3 itself. Additionally, the absorber temperature and therefore the Seebeck voltage decreases with increasing current which also affects the voltage output of the STEG.

Figure 6(b) shows the peak (current-optimized) thermoelectric efficiency as a function of the geometric parameter $C_{th}L$ for various cold-junction temperatures. Although the optimal geometric parameter is a function of the cold-junction temperature, the peak efficiency curves at a given cold-junction temperature are rather flat. At a cold-junction temperature of 25 °C, the maximum thermoelectric efficiency is 5% at $C_{th}L = 0.4\,\mathrm{m}$; at a cold-junction temperature of 100 °C, the maximum thermoelectric efficiency is 2.8% at $C_{th}L = 0.35\,\mathrm{m}$. The electrical power output of a unicouple STEG with a cold-junction temperature at 25 °C is 50 mW. For the chosen thermoelectric elements dimensions and a current price of approximately \$300/kg(Bi_2Te_3) the material cost can be estimated as $\sim 0.27\$/\mathrm{W_p}$. Further shrinking of the unicouple TEG to a length of 0.5 mm and the corresponding cross-sectional area of $\sim 1.14\,\mathrm{mm}^2$ to keep the optimal $C_{th}L$ for the same maximum STEG power output leads to material cost of $\sim \$0.03/\mathrm{W_p}$. Even the smaller thermoelectric elements are of a size that they can be produced with inexpensive bulk manufacturing process. The main cost of the unicouple TEGs will be the thermoelectric material.

The STEG efficiency is also sensitive to the incident solar radiation power. Figure 6(c) shows how the incident solar flux affects not only the efficiency of the STEG, but also the optimal value of the geometric parameter $C_{th}L$. The optimal geometric parameter $(C_{th}L)_{opt}$ decreases $(1.3 - 0.2\,\mathrm{m})$ with increasing solar insolation $(0.25 - 3\,\mathrm{kW/m^2})$. However, if the system is optimized for highest daily or all-year-round performance the $(C_{th}L)_{opt}$ will be slightly different due to the daily and yearly variation of the incident solar power. In order to optimize a STEG for maximum daily/all-year-round performance the accumulated electrical energy output of the STEG must be maximized. Figure 7 shows (a) the simulated solar intensity distribution for Boston over the course of a simulated sunny equinox day (September 22$^{\mathrm{nd}}$) (Bird and Riordan, 1984) and (b) the accumulated electrical energy output per day of a current-optimized STEG as a function of the $C_{th}L$. In those calculations the absorptance of the solar absorber is assumed to be independent of the incident angle of the solar radiation. For incident angles up to 60°, this

is a reasonable assumption for solar absorbers based on multilayer selective surfaces which are most commonly used for solar thermal applications (Tesfamichael and Waeckelgard, 2000). Additionally, possible shading effects occurring in a final design structure are neglected. For final device performance predictions those effects must be included. Independent of those details, the daily electrical performance of the STEG only depends weakly on $C_{th}L$ in a wide range $(0.35 - 0.8\,\mathrm{m})$ around the maximum of $0.3\,\mathrm{kWh/m^2/day}$. Consequently, within that range the $C_{th}L$ can be chosen for highest overall system efficiency if the STEG is integrated for example in a cogeneration or hybrid system(Kraemer et al., 2008) without significantly affecting the STEG performance.

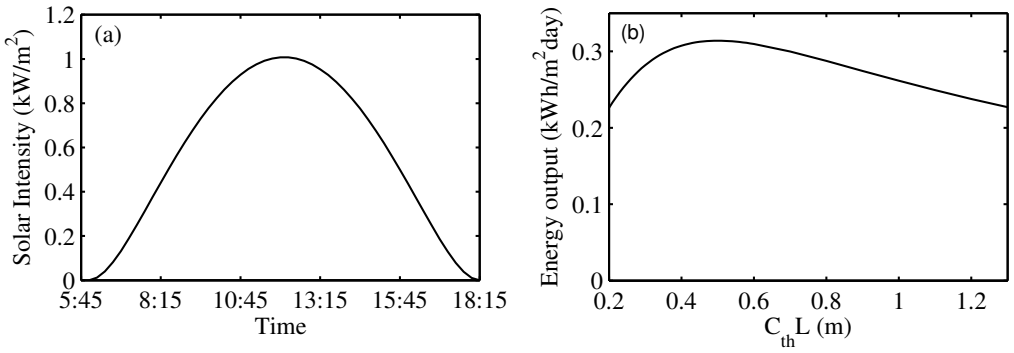

Figure 7: STEG optimization over the course of a day. (a) Simulated solar intensity distribution for Boston over the course of the day of September 22$^{\mathrm{nd}}$; (b) the accumulated electrical energy output per day of a current-optimized STEG as a function of the $C_{th}L$.

4.2. Rooftop electric power and hot water

In solar thermoelectric systems, approximately $50 - 80\%$ of the intercepted solar heat is released at the cold junction of the device as shown in Fig. 6(d). This waste heat must be removed in order to maintain the cold junction at a given temperature for the highest STEG performance. One way to remove this excess heat is first to spread it out on the cold side using a metallic heat spreader, and then to reject the heat to the environment via natural convection, similar to what is done for the heat management of PV cells. In certain applications such as cogeneration, this waste heat is actually the input to a secondary system such as a domestic hot water loop. Small deviations from the peak TEG operating point can have large (positive or

negative) effects on the quantity of heat delivered to the heat sink. As a result, a STEG cogeneration system can be designed to favor the production of either electrical power or waste heat, depending on the demands of the application. This can be accomplished by choosing the appropriate geometric parameter $C_{th}L$ (Fig. 6(b) and (d)). If it is desired to optimize the system for maximum electrical power then there is one specific optimal $(C_{th}L)_{opt}$ for a specific cold-junction temperature and incident solar flux as discussed in previous sections. Conversely, choosing a smaller $C_{th}L$ results in more heat transported to the hot water loop because the absorber stays at a lower temperature and thus the radiative heat losses of the system are smaller. Fortunately, as mentioned in the previous section, the daily total STEG electrical energy output is a weaker function of $C_{th}L$, so it is possible to deviate from the geometric parameter optimized for maximum electrical performance with only a negligible effect on the daily electrical performance.

For a system with fixed $C_{th}L$, it is even possible to adjust the balance between electrical power and waste heat solely by adjusting the electrical current of the circuit. As an example, we consider a system of $C_{th}L = 0.4\,\mathrm{m}$. Because the available excess heat and cold-junction temperature are both affected by the current, it is useful to plot the heat available for cogeneration per square meter of absorber area as a function of cold-junction temperature at various currents (Fig. 8). In those calculations the possible radiative heat losses from the back side of the copper heat sink to the glass enclosure (Fig. 1(a)) are taken into account and reduce the available heat for cogeneration. Superimposed on Fig. 8 are two sets of lines: red dashed lines are contour lines representing the corresponding STEG efficiency; blue dashed lines are the corresponding absorber temperature. This STEG operation diagram can be used to determine the conditions where the STEG can operate, because the performance of any heat sink can be characterized by its relationship between the heat sink temperature and the rejected heat. The constant of proportionality between the transferred heat and the temperature difference is the overall heat transfer coefficient, U in units W/K of the heat sink. In Fig. 8, dash-dotted lines of constant U are plotted in green for the example of a heat sink comprising a 25 °C fluid passing over the cold junction. Changing the electrical current allows the system to operate at different points along this heat transfer coefficient characteristic curve, affecting the cold-junction temperature, the amount of rejected heat, and the amount of electrical power generated. For example, if it is desirable to generate more waste heat in the morning and more electricity in the afternoon, it is possible

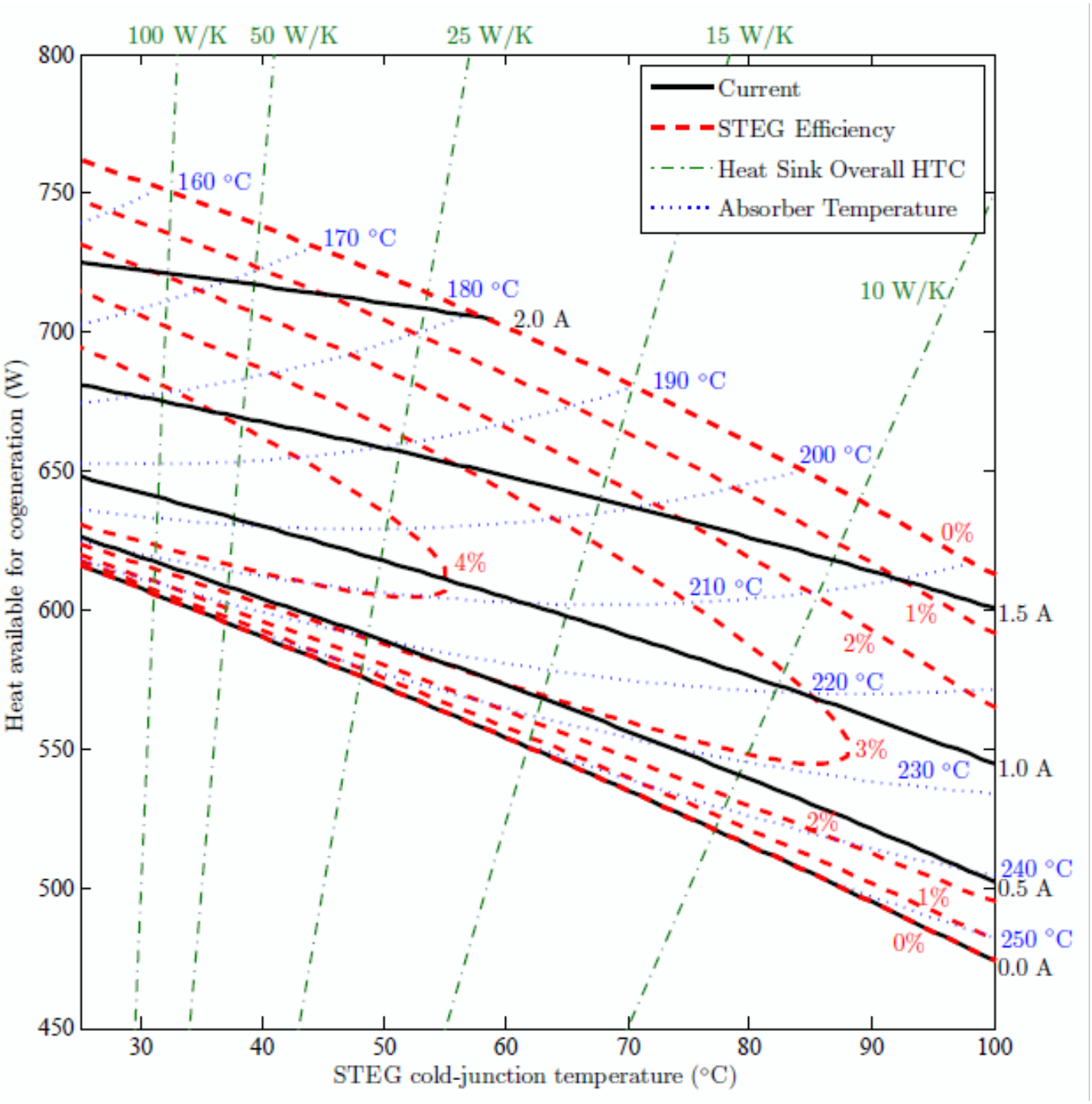

Figure 8: STEG Operation Diagram: Excess heat available for cogeneration at the cold junction of a STEG (optimized for 1 sun illumination, and cold-junction temperature of 25 °C) of 1 m^2 area under 1 kW/m^2 illumination as a function of the cold-junction temperature. Also shown are the STEG efficiency contour lines (dashed), STEG cell iso-current lines (solid), and the iso-overall-heat-transfer-coefficient (U) lines (dash-dotted).

to run the system in an "overdrive" mode (with super-optimal current) in the morning, and then run the system at optimal current in the afternoon. It is interesting to notice that there will always be two operational current points with the same STEG efficiency but with different cold-junction heat rejection rates if the STEG is operated at off-optimal conditions. For example for a heat sink with overall heat transfer coefficient of 25 W/K the line of constant U intersects the 4% efficiency contour line twice. One intersection corresponds to a current of approximately 0.8 A and the other one to 1.25 A. At the higher STEG current the effective conductance of the TEG increases due to thermal transport via electrons and holes, which results in a lower absorber temperature (198 °C). This decreases the radiation losses but also decreases the TEG conversion efficiency. These two effects result in less electricity generation, and more heat transported to the cold side (640 W). In addition, the cold-junction temperature increases slightly because of the assumed constant U-value. At the lower STEG current the effective conductance of the TEG decreases, resulting in a slightly lower cold-junction temperature, a higher absorber temperature (211 °C), and higher radiation losses, but a better TEG efficiency. The net result is the same 4% STEG efficiency, yet in this case less heat is transported to the cold side (605 W).

5. Conclusion

We developed a model and optimization methodology for earth-based STEG designs using a glass vacuum enclosure and a large flat-plate thermal concentration. A few assumptions are made and validated to present a simplified yet useful and realistic model for researchers and engineers who want to design STEGs or want to incorporate them in cogeneration systems. We describe, discuss and justify the necessary assumptions that have to hold for the STEG design to be independent of individual dimensions. The only geometric parameter which has to be optimized for highest STEG efficiency is $C_{th}L$, even if the temperature dependence of the thermoelectric materials and the solar absorber is included. This is a very useful result because it shows that the performance of a STEG is independent of the thermoelectric material volume, and the cost for the thermoelectric material can be negligibly small compared to the total system cost. The numerical simulations revealed that the optimal $(C_{th}L)_{opt}$ is weakly dependent on the cold-junction temperature, but shows a stronger dependence on the incident solar radiation. If the STEG efficiency is averaged over the course of a day only small

variations in the efficiency are observed in a wide range of $C_{th}L$ around the maximum. Consequently, if a STEG is integrated in a cogeneration system the $C_{th}L$ can be chosen within that range to optimize the overall efficiency without significantly affecting the STEG performance. For the matter of heat removal at the cold junction of the STEG cell we discussed the influence of the current on the released excess heat and the STEG efficiency and introduced a STEG operation diagram. This diagram illustrates the possible region of operation for the optimized STEG with a specific heat sink fluid temperature and solar insolation. The current is an additional parameter to actively optimize the operation of the cogeneration system and therefore the model underlying the STEG operation diagram can be used in controllers of those systems. The predicted efficiency for the Bi_2Te_3 based STEG considered in this paper is 5% at AM1.5G conditions and with a cold-junction temperature of 25 °C. With this efficiency and the concept of large thermal concentration the thermoelectric material cost can easily be reduced to below 0.05 \$/W_p and become negligible compared to the overall system cost. Consequently, integrating STEGs in solar hot water vacuum tube systems for cogeneration application shows potential to provide cost-competitively domestic hot water and electricity. However, more research and development is needed to explore this potential.

Acknowledgements

This material is based upon work supported by the Solid State Solar-Thermal Energy Conversion Center (S3TEC), an Energy Frontier Research Center funded by the U.S. Department of Energy, Office of Science, Office of Basic Energy Sciences under Award Number DE-SC0001299 [K.M., optical concentration, cogeneration]; and by the MIT-Masdar program [D.K., no/low optical concentration, loss modeling].

References

ASTM, 2008. Reference Solar Spectral Irradiances: Direct Normal and Hemispherical on 37° Tilted Surface. Technical Report ASTM Standard G 173-03. ASTM International.

Bird, R.E., Riordan, C.J., 1984. Simple solar spectral model for direct and diffuse irradiance on horizontal and tilted planes

at the earth's surface for cloudless atmospheres. Technical Report SERI/TP-215-2436. National Renewable Energy Laboratory. http://rredc.nrel.gov/solar/models/spectral/.

Buist, R.J., 1995. Calculation of peltier device performance, in: Rowe, D. M. (Eds.),CRC Handbook of Thermoelectrics, CRC Press LLC, Boca Raton, chap. 14.

Chen, G., 2011. Theoretical efficiency of solar thermoelectric energy generators. Journal of Applied Physics 109, 104908.

Chen, J., 1996. Thermodynamic analysis of a solar-driven thermoelectric generator. Journal of Applied Physics 79, 2717–2721.

Dent, C., Cobble, M., 1982. A solar thermoelectric generator experiments and analysis. Proc. 4th Inter. Conf. on Thermoelectric Energy Conversion , 75 – 78.

Domenicali, C.A., 1953. Irreversible thermodynamics of thermoelectric effects in inhomogeneous, anisotropic media. Physical Review 92, 877 – 881.

Duffie, J.A., Beckman, W.A., 2006. Solar Engineering of Thermal Processes. John Wiley & Sons, Inc, New Jersey. third edition.

Fuschillo, N., Gibson, R., Eggleston, F., Epstein, J., 1966. Solar thermoelectric generator for near-earth space applications. Electron Devices, IEEE Transactions on 13, 426 – 432.

Goldsmid, H., Giutronich, J., Kaila, M., 1980. Solar thermoelectric generation using bismuth telluride alloys. Solar Energy 24, 435 – 440.

Goldsmid, H.J., 1986. Electronic Refrigeration. Pion Limited, London.

Gupta, R.P., Xiong, K., White, J.B., Cho, K., Alshareef, H.N., Gnade, B.E., 2010. Low resistance ohmic contacts to bi_2te_3 using ni and co metallization. Journal of The Electrochemical Society 157, H666–H670.

Hogan, T., Shih, T., 2006. Modeling and characterization of power generation modules based on bulk materials, in: Rowe, D. M. (Eds.),Thermoelectrics Handbook Macro to Nano, CRC Press Taylor & Francis Group, Boca Raton, chap. 12.

Ioffe, A.F., 1957. Semiconductor thermoelements and thermoelectric cooling. Infosearch Limited, London.

Kennedy, C.E., 2002. Review of Mid- to High-Temperature Solar Selective Absorber Materials. Technical Report TP-520-31267. National Renewable Energy Laboratory.

Kraemer, D., Hu, L., Muto, A., Chen, X., Chen, G., Chiesa, M., 2008. Photovoltaic-thermoelectric hybrid systems: A general optimization methodology. Applied Physics Letters 92, 243503.

Kraemer, D., Poudel, B., Feng, H.P., Caylor, J.C., Yu, B., Yan, X., Ma, Y., Wang, X., Wang, D., Muto, A., McEnaney, K., Chiesa, M., Ren, Z., Chen, G., 2011. High-performance flat-panel solar thermoelectric generators with high thermal concentration. Nature Materials 10, 532538.

Li, P., Cai, L., Zhai, P., Tang, X., Zhang, Q., Niino, M., 2010. Design of a concentration solar thermoelectric generator. Journal of Electronic Materials 39, 1522–1530. 10.1007/s11664-010-1279-0.

Mahan, G.D., 1991. Inhomogeneous thermoelectrics. Journal of Applied Physics 70, 4551 – 4554.

Mills, A.F., 1999. Heat Transfer. Prentice Hall, Upper Saddle River. second edition.

Modest, M.F., 2003. Radiative Heat Transfer. Academic Press, Boston. second edition.

Poudel, B., Hao, Q., Ma, Y., Lan, Y., Minnich, A., Yu, B., Yan, X., Wang, D., Muto, A., Vashaee, D., Chen, X., Liu, J., Dresselhaus, M.S., Chen, G., Ren, Z., 2008. High-thermoelectric performance of nanostructured bismuth antimony telluride bulk alloys. Science 320, 634–638.

Rockendorf, G., Sillmann, R., Podlowski, L., Litzenburger, B., 1999. Pv-hybrid and thermoelectric collectors. Solar Energy 67, 227 – 237.

Rowe, D.M., 1981. A high performance solar powered thermoelectric generator. Applied Energy 8, 269 – 273.

Scherrer, H., Vikhor, L., Lenoir, B., Dauscher, A., Poinas, P., 2003. Solar thermolectric generator based on skutterudites. Journal of Power Sources 115, 141 – 148.

da Silva, L.W., Kaviany, M., 2004. Micro-thermoelectric cooler: interfacial effects on thermal and electrical transport. International Journal of Heat and Mass Transfer 47, 2417 – 2435.

Snyder, G.J., Ursell, T.S., 2003. Thermoelectric efficiency and compatibility. Phys. Rev. Lett. 91, 148301.

Telkes, M., 1954. Solar thermoelectric generators. Journal of Applied Physics 25, 765 – 777.

Tesfamichael, T., Waeckelgard, E., 2000. Angular solar absorptance and incident angle modifier of selective absorbers for solar thermal collectors. Solar Energy 68, 335 – 341.

Vatcharasathien, N., Hirunlabh, J., Khedari, J., Daquenet, M., 2005. Design and analysis of solar thermoelectric power generation system. International Journal of Sustainable Energy 24, 115 – 127.